



## Design and fabrication of biphasic cellular materials with transport properties – A modified bidirectional evolutionary structural optimization procedure and MATLAB program

Shiwei Zhou<sup>a,b</sup>, Joseph Cadman<sup>a</sup>, Yuhang Chen<sup>a</sup>, Wei Li<sup>a</sup>, Yi Min Xie<sup>b</sup>, Xiaodong Huang<sup>b</sup>, Richard Appleyard<sup>a</sup>, Guangyong Sun<sup>a</sup>, Qing Li<sup>a,\*</sup>

<sup>a</sup>School of Aerospace, Mechanical and Mechatronic Engineering, The University of Sydney, Sydney, NSW 2006, Australia

<sup>b</sup>Centre for Innovative Structures and Materials, School of Civil, Environmental and Chemical Engineering, RMIT University, GPO Box 2476, Melbourne 3001, Australia

### ARTICLE INFO

#### Article history:

Received 15 May 2011

Received in revised form 10 August 2012

Available online 18 September 2012

#### Keywords:

Homogenization

Heat and mass transport

Cellular materials

Topology optimization

Solid free-form fabrication

Stereo Lithographic Apparatus

### ABSTRACT

Heat and mass transfer in macellular materials signifies an important topic of research for a range of advanced applications such as in thermal, aerospace, geotechnical and scaffold tissue engineering etc. Based on the mathematical similarity of various transport problems, this paper proposes a modified bidirectional evolutionary structural optimization (BESO) method for design of biphasic microstructural composites with desirable transport properties. The cellular materials considered herein comprise periodic base cells and the homogenization technique is adopted to determine their effective (bulk) properties. The key is to optimize the topology of base cell model for minimizing the difference between the effective and target transport properties. Numerical examples agree well with the well-known benchmarking microstructures and some of them are prototyped using biphasic solid free-form fabrication (SFF) technology. To facilitate comprehension of the algorithm, a short MATLAB program is provided in the Appendix.

© 2012 Elsevier Ltd. All rights reserved.

### 1. Introduction

In the past two decades, great efforts have been directed towards the design and fabrication of novel cellular composites with extraordinary physical properties desired for special engineering applications [1,2]. One common basis of these studies resides in the fact that many natural and engineered composites are made up by periodic base cells (PBCs) or representative volume elements (RVEs). The compositions and microstructures of these PBCs determine the bulk material behaviors, making such composites particularly prevalent and attractive in material design when one or more specific requirements of physical properties are placed.

As an important computational tool in material development, the homogenization method [3] has proven particularly effective in finite element driven characterization and analyses [4]. The direct homogenization technique has been employed for microstructural material design, in which different compositions and/or configurations of PBC can be estimated and characterized computationally prior to costly physical prototyping and testing. To a certain extent, such a virtual trial-and-error exercise could help

accelerate the design process for a range of functional heat and mass transfer materials.

However, attaining the desired effective (or bulk) physical properties by tailoring the composition and/or microstructure of the candidate materials still remains rather challenging. A repeated use of the direct homogenization cannot guarantee that a specified physical property will be achieved and the computational cost of such a laborious trial-and-error procedure may become prohibitively high. For this reason, a more methodical approach has been required. Since the number of feasible PBC designs attaining a desired set of properties may be astronomical, the inverse homogenization method [2] has been developed to provide a more systematic procedure. This approach embeds the direct homogenization method within a topology optimization framework [1], where the design of the PBC microstructural layout is driven by an ongoing calculation of topological sensitivity of the difference between the homogenized and target properties. Thus, starting from an arbitrary initial design, the inverse homogenization method gradually redistributes the base materials such that the optimal microstructure configuration can be obtained for achieving desired physical properties. The design of multifunctional PBC materials for different physical properties could be found in a review article [5].

As a long-standing research topic, topology optimization aims to distribute specified quantities of multiphase materials for a

\* Corresponding author. Tel.: +61 2 93518607; fax: +61 2 93517060.

E-mail address: [Qing.Li@Sydney.edu.au](mailto:Qing.Li@Sydney.edu.au) (Q. Li).

range of single or multiple objective function(s). To formulate the topology optimization problem in a finite element framework, the volume fraction (or relative density)  $\rho(\mathbf{x})$  of the candidate material in each element is usually treated as the design variable, rendering the associated algorithms density-based. Although  $\rho(\mathbf{x})$  is expected to be 0/1 (white/black) in an element centered at point  $\mathbf{x}$ , it is usually relaxed to an intermediate value between 0 and 1 in mathematical programming or optimality criteria algorithms in order to avoid the ill-posed nature of the optimization problem. Nevertheless, such an intermediate variable is commonly penalized exponentially by a Solid Isotropic Material with Penalization (SIMP) method to ensure its convergence to either 0 or 1 in a final design [1]. In addition to this point-to-point approach, boundary-tracked model like level-set method [6] is capable of capturing the geometrical characterizations for the in-design structures and its applications to topology optimization have been reported in many literatures [7,8].

Over the last two decades, several topology optimization algorithms for density-based structural representation including Optimality Criteria (OC) [9], Genetic Algorithm (GA) [10] and Evolutionary Structural Optimization (ESO) [11–18] have proven effective and reached a level of maturity. Among them, the ESO method showed significant simplicity and effectiveness in multi-physics problems [19]. This method was based upon a simple concept of either removing redundant/inefficient materials from a structure [11] or shifting material from least efficient to most efficient location while maintaining the volume fraction [12,13]. The later version of ESO allows material alteration from two directions (i.e. adding and removing elements) simultaneously and is thus named bidirectional evolutionary structural optimization (BESO) [14–17,20]. Huang and Xie recently demonstrated successfully that BESO overtakes ESO in computational efficiency and robustness [16,21]. A modified BESO method was used to optimize the steady heat conduction problem under both design-independent and design dependent heat loads by Gao et al. in [22]. Compared with other topology optimization algorithms, ESO/BESO appears particularly simple in numerical implementation. In both ESO and BESO, the evolutionary process is driven by either relative stress level [11], performance index [23,24], or a full range of topological sensitivities [12], making this method considerably versatile. Its successful applications in elastic [11,12], thermal [25,26] and electromagnetic [19] structures inspires us to extend the BESO method from structural optimization to materials design for transport properties in this paper.

From an algorithmic perspective, the original BESO procedure allows altering material distribution in an element based fashion, where the entire candidate elements are added or removed in terms of the local sensitivity. This hard killing/restoring technique is effective in many benchmarking problems of structural optimization, where the difference of sensitivity is fairly significant. However, such an element-based procedure may result in severe oscillation of element removal and addition where the sensitivities are less distinct [27,28]. For instance, in material design a periodic base cell model is optimized where the sensitivity difference is not as significant as those in compliance-driven structural topology optimizations [29] and the inverse homogenization could often lead to multiple solutions of microstructures [30,31]. For these reasons, firstly, we would like to introduce a *soft-killing/restoring* scheme to BESO, in which only a part (rather than full) of material in each candidate element is altered according to the relative level of its sensitivity in each iteration. Secondly, the volume fraction is allowed to fluctuate around its constraint value. But the magnitude of the fluctuation diminishes to zero gradually with the convergence of the optimization.

In this paper, the Hashin-Strikman (HS) bounds [32] are taken as the target property for the PBC design. They are also used as the interpolation functions to calculate the local values in an ele-

ment mixed by two phase constituents. The sensitivity of the homogenized property is derived by using the adjoint variable method [33], followed by either the filter technique [34] or nonlinear diffusion techniques [35] to suppress checkerboard patterns in the optimal PBC structures. To demonstrate the capability of the modified BESO procedure in this study, several 2D and 3D illustrative examples are presented for the design of composites with the upper and lower HS bounds of transport properties. To demonstrate that the design results are manufacturable, some selected examples are fabricated with biphasic solid free-form fabrication (SFF) techniques, which have been used for rapidly prototyping complex 3D functional parts. A stand-alone MATLAB program is provided to facilitate the comprehension and implementation of the presented BESO material design method.

## 2. Statement of the problem

The cellular composites considered herein consist of self-repeated PBCs. Within such a RVE, the inverse homogenization problem is formulated to optimize the PBC microstructure so that the effective transport property of the composite approaches the target on the HS bounds. The mathematical details of the microstructural design problem, the target values, the effective transport property and the inverse homogenization are given as follows.

### 2.1. Effective transport property

Many physical field and transport problems, such as heat transfer, permeable flow, incompressible flow, electric conduction, diffusion, electrostatics and magnetostatics, etc. can be governed by the following quasi steady-state harmonic equation [36]

$$-\frac{\partial}{\partial x_i} \left( \kappa(\rho(\mathbf{x})) \frac{\partial T}{\partial x_j} \right) = q \quad i, j = 1, 2, 3 \quad \mathbf{x} \in \bar{\Omega} \quad (1)$$

where the local transport property  $\kappa(\rho(\mathbf{x}))$  depends on which constituent occupies the location  $\mathbf{x} = [x_1, x_2, x_3]^T$ . According to the homogenization theory [3], the field variable  $T$  can be asymptotically expanded to a polynomial consisted of global (macroscopic) field variable  $T^0(\mathbf{x})$  and local (microscopic) field variable  $T^i(\mathbf{x}, \mathbf{y})$ ,  $i = 1, 2, \dots$ , at the  $i$ th level of hierarchy of microstructure as below:

$$T(\mathbf{x}, \mathbf{y}) = \varepsilon^0 T^0(\mathbf{x}) + \varepsilon^1 T^1(\mathbf{x}, \mathbf{y}) + \varepsilon^2 T^2(\mathbf{x}, \mathbf{y}) + \dots \quad (2)$$

Without loss of generality, a two-level hierarchical composite is considered to simplify the derivation, where  $\mathbf{y} = [y_1, y_2, y_3]^T$  denotes the microscopic (local) coordinate system relating to its macroscopic (global) counterpart  $\mathbf{x} = [x_1, x_2, x_3]^T$  by a scale factor  $0 < \varepsilon \ll 1$ , given as  $\mathbf{x} = \varepsilon \mathbf{y}$ . To calculate the derivative with respect to the macroscopic coordinate  $\mathbf{x}$ , the chain rule is applied to  $\mathbf{x} = \varepsilon \mathbf{y}$ , leading to the differentiation across these two scales as

$$\frac{\partial}{\partial \mathbf{x}} = \frac{\partial}{\partial \mathbf{x}} + \frac{\partial}{\partial \mathbf{y}} \frac{\partial \mathbf{y}}{\partial \mathbf{x}} = \frac{\partial}{\partial \mathbf{x}} + \frac{1}{\varepsilon} \frac{\partial}{\partial \mathbf{y}} \quad (3)$$

Substituting asymptotically-expanded  $T$  and differential operator  $\partial/\partial \mathbf{x}$ , defined in Eqs. (2) and (3) respectively, into Eq. (1), arranging the terms based on the exponent of  $\varepsilon$  and extracting the terms in terms of the order of  $\varepsilon^{-1}$ , we obtain

$$\frac{\partial}{\partial x_i} \left( \kappa \frac{\partial T^0}{\partial y_j} \right) + \frac{\partial}{\partial y_i} \left( \kappa \frac{\partial T^0}{\partial x_j} \right) + \frac{\partial}{\partial y_i} \left( \kappa \frac{\partial T^1}{\partial y_j} \right) = 0 \quad (4)$$

According to Eq. (2),  $T^0$  does not depend on  $\mathbf{y}$ , leading to  $\partial T^0 / \partial y_j = 0$ . Thus the first term in Eq. (4) can be dropped, yielding

$$\frac{\partial}{\partial y_i} \left( \kappa \frac{\partial T^1}{\partial y_j} \right) = -\frac{\partial}{\partial y_i} \left( \kappa \frac{\partial T^0}{\partial x_j} \right) = -\frac{\partial T^0}{\partial x_j} \frac{\partial \kappa}{\partial y_i} \quad (5)$$

According to the Taylor series, periodic field variable  $T^1$  can be assumed as the macro field variable  $T^0(\mathbf{x})$  minus the multiplication of the micro-scale periodic characteristic field variable  $\chi(\mathbf{y})$  and the macro-scale-based gradation of  $T^0(\mathbf{x})$ ,

$$T^1 = T^0(\mathbf{x}) - \chi(\mathbf{y}) \frac{\partial T^0}{\partial \mathbf{x}} \quad (6)$$

Differentiating Eq. (6) with respect to  $\mathbf{y}$  leads to

$$\frac{\partial T^1}{\partial y_j} = - \frac{\partial \chi(\mathbf{y})}{\partial y_j} \frac{\partial T^0}{\partial x_j} \quad (7)$$

Inserting Eq. (7) into Eq. (5), we finally obtain

$$\frac{\partial}{\partial y_i} \left( \kappa \frac{\partial \chi(\mathbf{y})}{\partial y_j} \right) = \frac{\partial \kappa}{\partial y_i} \quad (8)$$

The solution to Eq. (8) is called the characteristic field  $\chi(\mathbf{y})$ , which is the key to the homogenization-based calculation of the effective transport properties [37].

Extracting the  $\varepsilon^0$  terms in the extension of Eq. (1), we obtain

$$- \left[ \frac{\partial}{\partial x_i} \left( \kappa \frac{\partial T^0}{\partial x_j} \right) + \frac{\partial}{\partial x_i} \left( \kappa \frac{\partial T^1}{\partial y_j} \right) \right] = q \quad (9)$$

According to Eq. (7), we replace  $\partial T^1 / \partial y_j$  with  $-\partial \chi(\mathbf{y}) / \partial y_j \partial T^0 / \partial x_j$ , and finally obtain

$$- \frac{\partial}{\partial x_i} \left( \kappa \left( \mathbf{I} - \frac{\partial \chi(\mathbf{y})}{\partial y_j} \right) \frac{\partial T^0}{\partial x_j} \right) = q \quad (10)$$

Eq. (10) has a similar form to the original harmonic equation as Eq. (1) except the base transport property  $\kappa$  is replaced by  $\kappa(\mathbf{I} - \partial \chi(\mathbf{y}) / \partial y_j)$ . According to the homogenization theory, as  $\varepsilon \rightarrow 0$ ,  $\kappa(\mathbf{I} - \partial \chi(\mathbf{y}) / \partial y_j)$  approximates an average value integrated over the PBC domain. Therefore the effective transport property can be defined as

$$\bar{\kappa} = \frac{1}{|\Omega|} \int_{\Omega} \kappa \left( \mathbf{I} - \frac{\partial \chi}{\partial \mathbf{y}} \right) d\Omega \quad (11)$$

where  $|\Omega|$  denotes the volume of the PBC domain and  $\mathbf{I}$  stands for the second-order (2D) or third-order (3D) identity. The formulation of Eq. (11) in a finite element framework can be expressed as,

$$\bar{\kappa}_{ij} = \frac{1}{|\Omega|} \sum_{e=1}^{NE} \left( \kappa_{ij}^e \left( 1 - \frac{\partial \chi_i^e}{\partial y_j} \right) |\Omega^e| \right) \quad (12)$$

where the symbols with superscript  $e$  indicate that they are valued at element level (e.g.  $|\Omega^e|$  denote the volume or area of the local element, respectively, in 3D and 2D cases). It is noted that the effective thermal conductivity can be calculated by other methods. For example, the effective parameter can be obtained by averaging the steady heat flux through the cross section area of the media over the temperature difference within a given distance [38]. But such method seems inappropriate for the following inverse design process in the topology optimization framework.

## 2.2. Hashin-Strikman bounds

The transport properties like conductivity, diffusivity or permeability are used to measure the material's capability of transferring energy or mass from one point to other. It is usually a second-order positive definite tensor denoted by two eigenvalues  $\lambda_1$  and  $\lambda_2$  in 2D cases, as

$$\kappa = \begin{bmatrix} \lambda_1 & 0 \\ 0 & \lambda_2 \end{bmatrix} \quad (13)$$

For a biphasic isotropic composite, these two eigenvalues are equal ( $\lambda = \lambda_1 = \lambda_2$ ), thus the transport properties for phases one and two are denoted as  $\kappa_1 = \eta_1 \mathbf{I}$  and  $\kappa_2 = \eta_2 \mathbf{I}$ , respectively. The allowable eigenvalues mainly depend on the compositional properties, volume fractions and microstructures of the material constituents. A range of estimated bounds only taking the first two factors into consideration for the admissible eigenvalues have been proposed. In this regard, the well-known Wiener bounds are perhaps the simplest [39], given as

$$\left( \frac{c}{\eta_1} + \frac{(1-c)}{\eta_2} \right)^{-1} \leq \lambda \leq c\eta_1 + (1-c)\eta_2 \quad (14)$$

where  $c$  and  $1-c$  are the volume fractions for phase 1 and phase 2, respectively. As the Wiener bounds are too wide to be attained [30], Hashin and Strikman developed much tighter (HS) bounds to narrow the admissible domain, originally for conductivities in 2D and 3D [32]. If  $\eta_1 < \eta_2$ , the two-dimensional and three-dimensional HS bounds are respectively given by

$$-\eta_1 + \left( \frac{c}{2\eta_1} + \frac{1-c}{\eta_1 + \eta_2} \right)^{-1} \leq \lambda \leq -\eta_2 + \left( \frac{c}{\eta_1 + \eta_2} + \frac{1-c}{2\eta_2} \right)^{-1} \quad \text{in 2D} \quad (15)$$

$$\eta_1 + \frac{3(1-c)\eta_1(\eta_2 - \eta_1)}{3\eta_1 + c(\eta_2 - \eta_1)} \leq \lambda \leq \eta_2 + \frac{3c\eta_2(\eta_1 - \eta_2)}{3\eta_2 + (1-c)(\eta_1 - \eta_2)} \quad \text{in 3D} \quad (16)$$

In addition to serving as the target values, the HS bounds are the ideal interpolation functions for estimating the local transport property when an element is mixed with two phases of constituent materials. Indeed, the commonly-used interpolation schemes are mainly based on the Wiener bounds where the local density needs to be exponentially penalized for ensuring its convergence to 0 or 1 in the final topology. As the HS bounds are much closer to the real values, the design variables can converge to their extreme values without need of penalty. Furthermore, to ensure the problem non-trivial, the interpolation scheme should be different from the target value. That is to say, if the target is on the lower HS bound, the upper HS bound should be employed as the interpolation function, and *vice versa*.

## 2.3. Objective function and sensitivity analysis

After defining the effective transport properties and their allowable extreme values, the design problem becomes how to make the effective (or homogenized) values ( $\bar{\kappa}$ ) attain their targets ( $\hat{\kappa}$ ) by distributing the candidate materials within the base cell. Mathematically, this problem can be formulated in terms of the minimization of a positive potential energy, equivalent to the summation of the least squares of the difference between corresponding entries in these two quantities, given by

$$\min_{\rho^e} J(\rho^e) = \sum_{ij=1}^2 r_{ij} (\hat{\kappa}_{ij} - \bar{\kappa}_{ij})^2 \quad (17)$$

subject to  $\int_{\Omega} \rho^e d\Omega = V_0$

where  $V_0$  denotes the volume constraint for one material and  $r_{ij}$  acts as the weighting factor to emphasize or balance the role of different entries in the objective function. Such weighting factors are usually equal to 1 for isotropic examples given in this paper but might be different for anisotropic cases. The local volume fraction  $\rho^e$  in each candidate element is taken as the design variable. For 2D cases, the sensitivity of the objective function with respect to the design variable can be expressed as,

$$\alpha^e = \frac{\partial J}{\partial \rho^e} \approx \frac{\Delta J}{\Delta \rho^e} = -2 \sum_{ij=1}^2 r_{ij} (\hat{\kappa}_{ij} - \bar{\kappa}_{ij}) \left( 1 - \frac{\partial \chi_i}{\partial y_j} \right) \frac{\Delta \bar{\kappa}_{ij}}{\Delta \rho^e} \left( 1 - \frac{\partial \chi_j}{\partial y_i} \right) \quad (18)$$

where  $\alpha^e = \partial J / \partial \rho^e \approx \Delta J / \Delta \rho^e$  denotes the gradient of the variation in the objective function,  $\Delta J$ , to the variation in volume fraction,  $\Delta \rho^e$ .

As a criterion to assess which element should be changed in the BESO procedure, however, the sensitivity in Eq. (18) is often not directly used as it commonly results in checkerboard patterns, where some regions are occupied by different phases alternately. In this regard, the filter technique [34] has proven effective in structural topology optimization to eliminate such numerical instability, where the local sensitivity  $\alpha^e$  at each element is replaced by an averaging value in all its adjacent elements. But it might be malfunction in material design as the sensitivity in Eq. (18) may not be sensitive enough in some cases [29–31]. As a new attempt, the nonlinear diffusion method is introduced into the BESO method, in which an extra term weighted by a positive factor  $\zeta$  is added to the objective function as below

$$J(\rho) = \sum_{ij=1}^2 r_{ij} (\hat{\kappa}_{ij} - \bar{\kappa}_{ij})^2 + \zeta \int_{\Omega} \varphi(\|\nabla \rho\|) d\Omega \quad (19)$$

The sensitivity of the diffusion energy (the second term in Eq. (19)) with respect to the relative volume fraction  $\rho$  is given by

$$\frac{\partial \varphi(\|\nabla \rho\|)}{\partial \rho} = -\text{div} \left[ \frac{\partial \varphi}{\partial (\|\nabla \rho\|)} \frac{1}{\|\nabla \rho\|} \nabla \rho \right] \quad (20)$$

where  $\text{div}$  denotes the divergence of a vector. Derived from the Fick's law and continuity condition, the diffusion process was firstly used to describe mass transport. Different diffusion functions determine different diffusion processes. For example, if  $\varphi(\|\nabla \rho\|) = 1/2 \|\nabla \rho\|^2$ , the right side of Eq. (20) degenerates to the well-known Laplace operator, which coincides with the linear filter models in topology optimization [35]. With the introduction of the nonlinear diffusion energy, the sensitivity finally becomes

$$\alpha^e = -2 \sum_{ij=1}^2 (\hat{\kappa}_{ij} - \bar{\kappa}_{ij}) \left( 1 - \frac{\partial \chi_i}{\partial y_j} \right) \frac{\Delta \bar{\kappa}_{ij}}{\Delta \rho^e} \left( 1 - \frac{\partial \chi_j}{\partial y_i} \right) - \zeta \text{div} \left[ \frac{\partial \varphi}{\partial (\|\nabla \rho^e\|)} \frac{1}{\|\nabla \rho^e\|} \nabla \rho^e \right] \quad (21)$$

#### 2.4. The modified bidirectional evolutionary structural optimization (BESO)

The original evolutionary structural optimization (ESO) method [11–17] was unidirectional, which only allows removing redundant materials from a fully-occupied structure. As such, the volume of the solid phase decreases monotonically, making it impossible to replenish improperly removed materials and sometimes resulting in an overly-killed structure. To deal with this problem, a thickness-based morphing technique was developed to enable concurrent addition and removal of material within each iteration. Lately, a bi-directional structural optimization method (BESO) capable of adding and removing elements simultaneously was proposed [20], which quickly showed its superior effectiveness and robustness over the traditional ESO method for a range of structural optimization problems [16].

Although BESO demonstrates its versatility in generating more reliable topology as well as making the optimization more independent on the initial designs [20], its search capability could be limited by the addition and removal of whole elements in each iteration. The alteration of whole candidate elements from either

solid to void (hard-kill) or void to solid (hard-revive) happens in high stress or sensitivity concentration regions, sometimes making convergence problematic. In some cases, the presence and absence of some elements occurs in an oscillatory fashion and often a regulation of design parameters is required [27]. Furthermore, the traditional BESO procedure has no control on the number of elements added and deleted in each iteration, making the prescription of a volume constraint difficult [20].

One method to remedy this malfunction is what was named “soft-kill” or “soft-revive” by downgrading or upgrading the material (in terms of volume fraction) partially in each element [12,13,40], as  $\rho_{k+1}^e = \max(\rho_{\min}, \min(1, \rho_k^e \pm \bar{\rho}))$ , where  $0 < \rho_{\min} \ll 1$  is a small positive number to avoid singularity in finite element analysis and  $\bar{\rho}$  is a prescribed constant defining the step-size of updating design variables. Compared to the well-known SIMP method, the relaxation of the design variable in such a BESO method is incomplete because the updated volume fraction  $\rho_{k+1}^e$  varies in a step-wise fashion by taking two extreme bounds of the set,  $\{\rho_{k+1}^e | \max(\rho_{\min}, \min(1, \rho_k^e - \bar{\rho} \leq \rho^e \leq \rho_k^e + \bar{\rho}))\}$ , other than its whole domain. As there are only two admissible values for  $\rho_{k+1}^e$ , it is really important to find a proper step-size  $\bar{\rho}$  so that the BESO method is neither too “hard”, where an overly-large step-size may lead to  $\rho_{k+1}^e = \rho_{\min}$  or 1, like the traditional element-based BESO, nor too “soft”, where an overly-small step-size results in an insignificant updating.

We here attempt to improve the traditional thickness and element-based BESO method [20] from two perspectives. Firstly, the volume constraint is relaxed, meaning that there is no strict restriction in maintaining the same volume in each iteration. Specifically, two sets of elements are determined in terms of their algebraic ranking in sensitivities: (1) the upper sensitivity set, whose corresponded elements will be weakened or downgraded, and (2) the lower sensitivity set, whose corresponding elements will be strengthened or upgraded. These two sets of elements keep changing during the iteration, depending on the thresholds in each step (e.g.  $(1 - \delta)\alpha_{mean}$  and  $(1 + \delta)\alpha_{mean}$  in terms of the mean sensitivity  $\alpha_{mean}$  and threshold coefficient  $\delta$ ). Within the upper sensitivity set, the volume fraction of candidate element will be decreased if the volume fraction is greater than its constraint  $V_0$ . In contrast, the volume fraction of candidate elements in the lower sensitivity set will be increased if the volume fraction is smaller than constraint  $V_0$ . The implementation of this evolution process is given as line 29 to 48 in the appended MATLAB code. It should be mentioned here that the strengthening and weakening sets should be swapped if the upper HS bound is taken as the target. Because the effective property obtained from the homogenization is based on the real volume fraction in each step, the target in the BESO algorithm should be changed in terms of this real value other than the initial volume constraint  $V_0$ . The relaxation of the volume fraction reduces gradually, i.e., the difference between the constraint and the real volume will diminish to zero and its influence on the target becomes trivial.

The second improvement in the BESO method consists in that step-size  $\bar{\rho}$  is no longer a constant (as in the thickness morphing [12,13]), but a gradually decreased value defined by  $\bar{\rho}_{k+1} = \mu \bar{\rho}_k$  (where  $\mu = 0.9000 \sim 0.999$  with an initial step-size, e.g.  $\bar{\rho}_0 = 10\%$ ) as the evolution progresses. Such a dynamic change in the step-size provides adequate flexibility and effectiveness, where the design can more quickly approach to a topological sketch near the optimum in the beginning. As the design evolves, the changed step-size allows the PBC structure gradually converging to its optimum and the volume constraint in the end. To have a clear view of this new BESO procedure, a simple MATLAB code is provided in Appendix A for design of a 2D biphasic microstructural composite targeting on the lower HS bound property.

### 3. Results and discussion

The following examples aim to demonstrate the capabilities of the proposed modification of the BESO method for the design of cellular materials both in 2D and 3D. A number of design parameters are used in the MATLAB code. Firstly, the design domain is assumed to be a rectangle discretized into an  $n_x \times n_y$  mesh with 4-node square elements or into an  $n_x \times n_y \times n_z$  mesh with 8-node cubic elements in 2D and 3D, respectively. In all the figures illustrating microstructures below, black (dark) and green (light) colors denote the materials with lower ( $\kappa_1 = 1$ ) and higher ( $\kappa_2 = 31$ ) base transport properties, respectively. Unless otherwise stated, the volume fraction is set  $V_0 = 0.5$  so that the lower and upper HS bounds used as the targets are  $\kappa^{\text{LHS}} = 1.667\mathbf{I}$  and  $\kappa^{\text{UHS}} = 1.800\mathbf{I}$  in 2D and  $\kappa^{\text{LHS}} = 1.750\mathbf{I}$  and  $\kappa^{\text{UHS}} = 1.875\mathbf{I}$  in 3D. The weighting factors for the different entries of objective property tensor are equal to  $r_{ij} = 1$  in all the examples.

To conduct a proper sensitivity analysis, initial values need to involve a non-uniform material distribution. In this study, three different initial designs are considered: (1) Initial Design I, whose the pixel/voxel (i.e. elemental) volume fraction distribution is proportional to the distance from the pixel/voxel center to the base cell center, as plotted in Fig. 1a; (2) Initial Design II, whose the volume fraction distribution is inversely proportional to that distance as in Fig. 1b; and (3) Initial Design III (Fig. 1c), whose volume fraction is defined in Line 5 in the appended MATLAB code.

#### 3.1. 2D examples targeting for the lower HS bound

The first example (Example 1) is carried out within a squared base cell discretized into  $n_x \times n_y = 200 \times 200$  elements. Starting from the Initial Design II, the effective property converges to  $\text{diag}(\bar{\kappa}) = [1.6811, 1.6806]^T$  (diag. denotes the diagonal entries of a matrix), fairly close to the targeted HS lower bound of  $\bar{\kappa} = \kappa^{\text{LHS}} = 1.6667\mathbf{I}$  after 150 iterations. The volume fraction of the optimal structure in Fig. 2a is exactly equal to the constraint of  $V_0 = 0.5$ . By ranking the base cells repeatedly in 2D space, a bi-connected low transport phase (black) is obtained in Fig. 2c, forming a matrix separating the high transport phase (light green). It is found that the high transport phase takes a circular shape. Such a Vigdergauz-like structural microstructure are also found to attain the upper HS bulk modulus [41], maximal permeability [42] and thermal conductivity by the MMA method [30].

Starting from Initial Design III (Example 2), the base cell design converges to a slightly different topology shown in Fig. 2b, which provides other optimal microstructure for the lower HS bound. The final effective transport property is  $\text{diag}(\bar{\kappa}) = [1.6759, 1.6737]^T$ . Its self-repeated assembly in Fig. 2d is actually the well-known Kagomé-like lattice in materials science [43]. In fact such

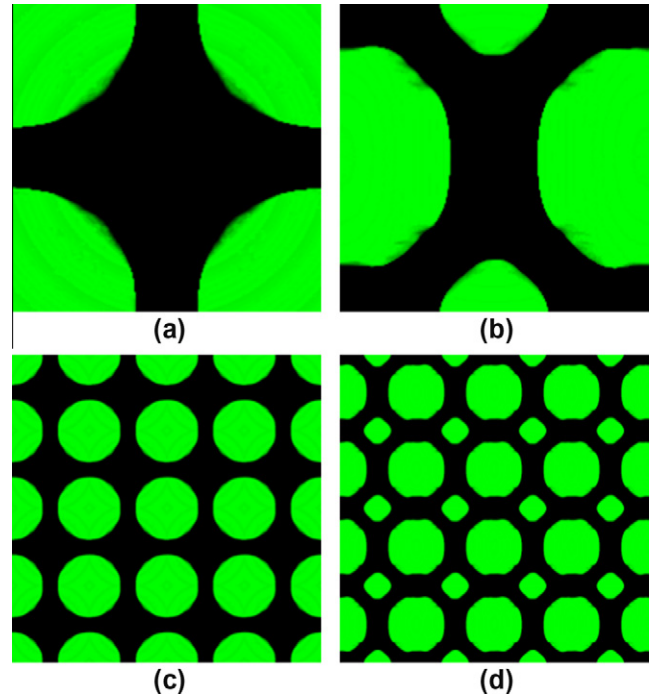


Fig. 2. Biphase microstructure of a cellular composite targeting for the lower HS bound (a) Optimal base cell with width:height = 1:1 starting from initial values II (Example 1); (b) Optimal base cell with width:height = 1:1 starting from initial values III (Example 2); (c) Base cell in (a) ranking in a  $4 \times 4$  matrix; (d) Base cell in (b) ranking in a  $4 \times 4$  matrix.

a high-transport cellular structure has been widely-reported being of extraordinary properties in magnetic [44], superconducting [45], percolating and elastic fields.

Fig. 3 illustrates the convergence of the objective function and volume fraction for Examples 1 and 2, in which the objective drops drastically in the first 20 iterations and converges to zero within 100 iterations. Compared to the objective function, the volume fraction converges in a different way that oscillates around the constraint in the beginning but finally approaches 0.5. A corresponding MATLAB code is provided for Example 2 in the Appendix, which is initiated by simply entering BESO(200,200,0.5,0.12,0.1,1,1,1,3,0.05) in the MATLAB prompt window. Indeed, by changing the initial design and/or the shape of design domain, different results can be generated as below. More details about this example code are provided in the Appendix.

In Examples 3 and 4, the aspect ratio of the width to height of the base cell is deliberately set to 3:1 to observe its effect on the attained effective transport property. To make use of typical square

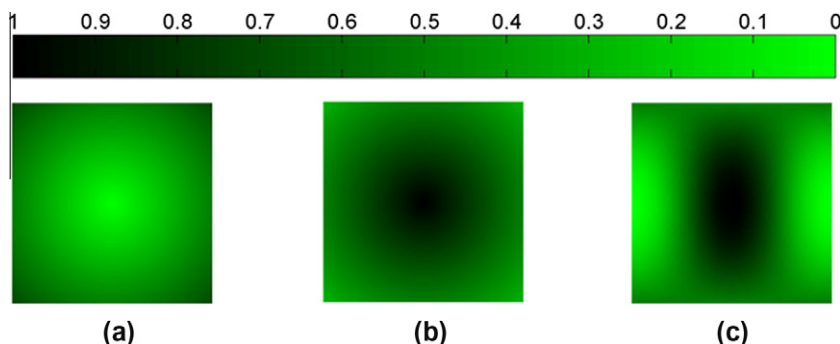


Fig. 1. Initial microstructures: (a) Initial Design I; (b) Initial Design II. (c) Initial Design III.

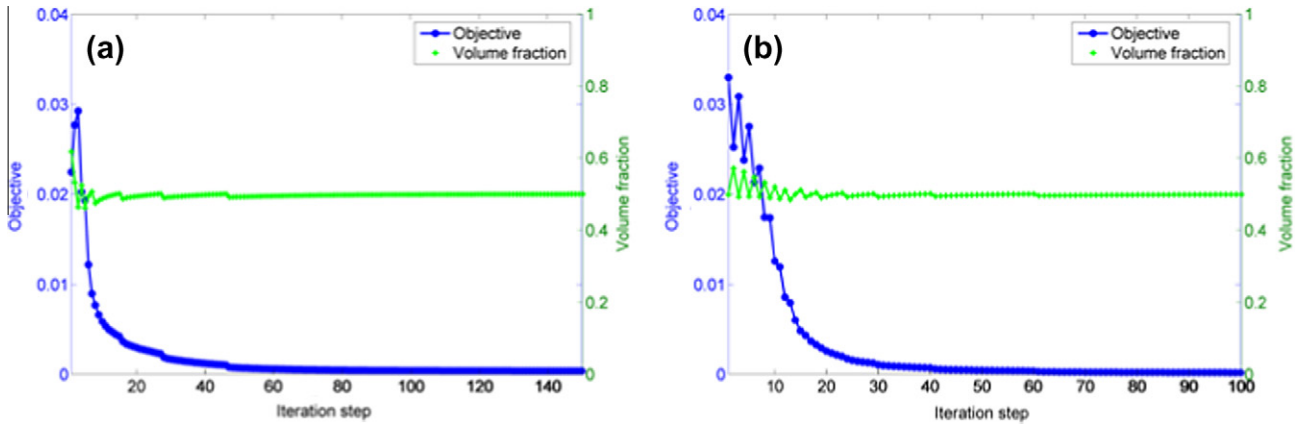


Fig. 3. The convergence of the objective function and volume fraction in (a) Example 1; (b) Example 2.

elements, the design domain (base cell) are modeled by a mesh of  $n_x \times n_y = 300 \times 100$ . For Examples 3 and 4, three squared Initial Designs II and I are evenly placed in this 3:1 rectangular base cell domain, respectively. Since most design parameters, except for the shape of design domains, are the same as those in Examples 1 and 3, the optimal base cells as shown in Fig. 4a are actually three horizontally-repeated base cells (similar to Fig. 2a). Although the optimal microstructures of PBCs seem much different, they do have almost the same effective property ( $\bar{\kappa} = 1.67931$  for Fig. 4a,  $\bar{\kappa} = 1.68071$  for Fig. 4b and  $\text{diag}(\bar{\kappa}) = [1.6787, 1.6778]$  for Fig. 4c). More interestingly, the composites constructed by the base cells in Figs. 4a,b actually have the identical microstructures when they are periodically assembled as shown in Figs. 4d,e. Also Fig. 4f has the same topology as that in Fig. 2d.

3.2. 2D examples targeting for the upper HS bound

This section presents two other examples (Examples 6 and 7) for the cellular materials targeting on the upper HS bound. In these examples, the “German-McClure” function  $\phi(s) = (1 + s^2) - 2$  is chosen as the diffusion function for its proven capability in structural topology optimization with the SIMP method [35]. The design domain in Example 5 is a square discretized by  $n_x \times n_y = 200 \times 200$  elements and the design starts from Initial Design I. Compared with the optimal microstructure shown in Fig. 2a, the result in

Fig. 5a illustrates the areas occupied by low-transport phase are now occupied by the high-transport phase, and vice versa. This phenomenon that swapping the properties of constituent material changes its effective value from the lower/upper to upper/lower HS bound has been reported in [29,30,46]. Fig. 5c shows that the high-transport phase in the upper HS bound composite is continuous while its counterpart in the lower bound is separated into evenly-distributed circular inclusions. The volume fraction of the optimal microstructure in Fig. 5a is also 0.5 and the attained effective value for this example is  $\bar{\kappa} = 1.79861$ , fairly close to the target of  $\hat{\kappa} = 1.8001$ .

To observe the effect of the shape of base cell on the cellular material with the upper bound property, Example 6 is made up of a 3:1 rectangular domain. Two identical patterns similar to Initial Design I are placed as the initial design in the rectangular PBC domain. An optimal PBC microstructure is shown in Fig. 5b, in which a horizontal high-transport bar is formed to connect the two Greek crosses as in Fig. 5b. From Fig. 5d, we found that the low-transport phase accumulates in two shapes, namely big and small rectangular inclusions with round corners. The high-transport phase is well connected in Example 6, making the effective property  $\bar{\kappa} = 1.79841$ , nearly attaining its target  $\hat{\kappa} = 1.8001$ . These 2D examples clearly supports the claim by Carson et al. [47] that isotropic porous materials should be divided into internal and external porosity materials, in which optimal heat transfer path-

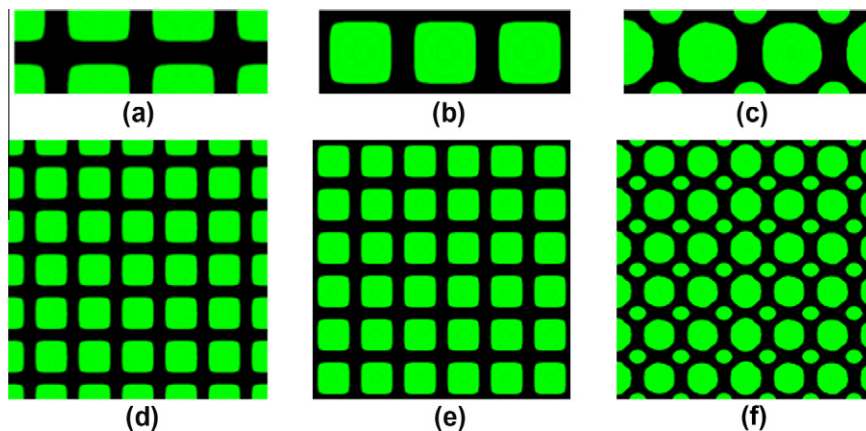
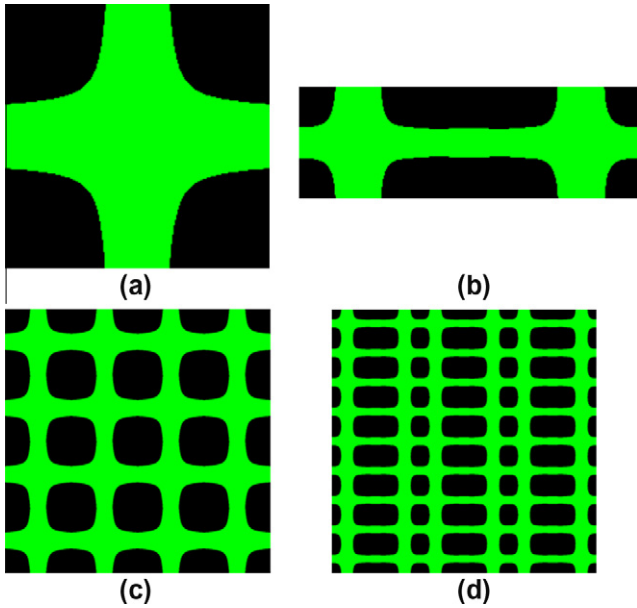


Fig. 4. The microstructure (width:height = 3:1) of a composite targeting for the lower HS bound (a) Optimal base cell starting from initial values II (Example 3); (b) Optimal base cell starting from initial values I (Example 4); (c) Optimal base cell starting from initial values III (Example 5); (d) Base cell in (a) ranking in a  $2 \times 6$  matrix; (e) Base cell in (b) ranking in a  $2 \times 6$  matrix; (f) Base cell in (c) ranking in a  $2 \times 6$  matrix.



**Fig. 5.** The microstructure of a composite targeting for the upper HS bound (a) Optimal base cell with width:height = 1:1 starting from Initial Design I (Example 6); (b) Optimal base cell with width:height = 3:1 starting from Initial Design I (Example 7); (c) Base cell in (a) ranking in a 4 × 4 matrix; (d) Base cell in (b) ranking in a 3 × 9 matrix.

way is through the continuous and dispersed phases, respectively. The benchmarking examples validate the effectiveness of the presented BESO method in 2D cellular material design. Furthermore, with different initial designs, the modified BESO can yield different solutions, reflecting an important nature of the inverse homogenization technique, i.e. different microstructures can attain the same or close physical properties.

The application of BESO method in structural topology optimization and other fields have been reported extensively, but its usage in

material design is rare. To demonstrate a better performance of this modified BESO method than more traditional BESO approach [20,27], Example 2 is re-run by adding or deleting the entire element in each iteration. Because the density is strictly limited to 0 or 1, the abovementioned initial structures with intermediate densities have to be discarded in traditional BESO. For this purpose, two different dark-green initials (cross-like and square structures as shown in Fig. 6a and 6end e) are used in Examples 8 and 9. To ensure numerical stability, around 1% of the total elements is allowed to be updated in each iteration. The rest parameters of these two examples are the same as those used in Example 2.

The snapshots in Fig. 6b–d and Fig. 6f–h illustrate the evolution process. Both of optimal structures (as shown in Fig. 6d and h) in Examples 8 and 9 have lattice-like structures and look apparently unsymmetrical even though starting from symmetrical initials. The convergence histories for these two examples in Fig. 7 show that the optimization is fairly slow, especially in the later stage. The objectives seem converging to zero but the effective conductivities,  $\text{diag}(\bar{\kappa}) = [1.7045, 1.7022]$  and  $\text{diag}(\bar{\kappa}) = [1.6980, 1.6960]$  respectively, are higher than their counterpart in the modified BESO,  $\text{diag}(\bar{\kappa}) = [1.6759, 1.6737]$  in Example 2, and the target  $\hat{\kappa} = \kappa^{LHS} = 1.6667\mathbf{I}$ . It is believed that the disadvantages of traditional BESO algorithm attribute to the strict constraints in both elemental density and volume fraction, which are relaxed to continuous functional spaces in the modified BESO method. Thus the numerical feasibility and flexibility are improved considerably.

### 3.3. 3D examples targeted for the lower HS bound

The extension of the material design from 2D to 3D presents no significant theoretical difficulties. However, due to limitations in the computing power available, the mesh size for the following 3D examples is set as  $n_x \times n_y \times n_z = 40 \times 40 \times 40$ .

For the lower HS bounds (Example 10), the high-transport phase (light green) is evenly distributed in a shape of cubic with round corners in the composite (Fig. 8a). To have a clear view of the microstructure, a RVE is extracted from the center of  $2 \times 2 \times 2$

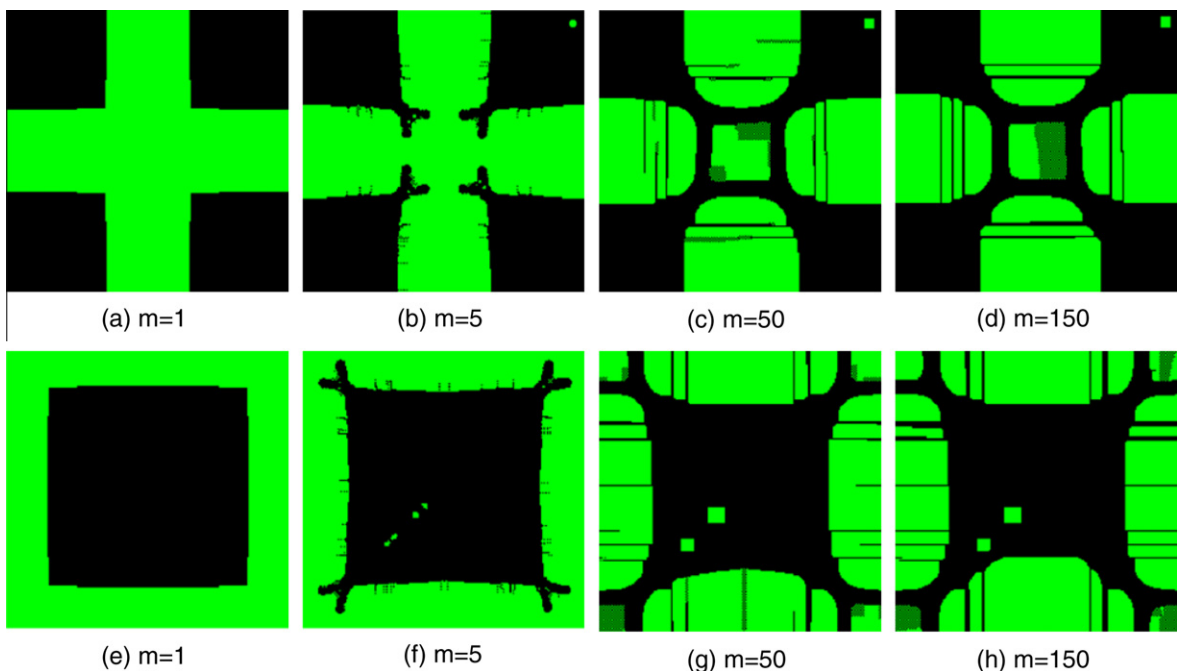


**Fig. 6.** The snapshots of the optimization with traditional BESO method starting from: (a)–(d) cross-like structure (Example 8); (e)–(h) square structure (Example 9).

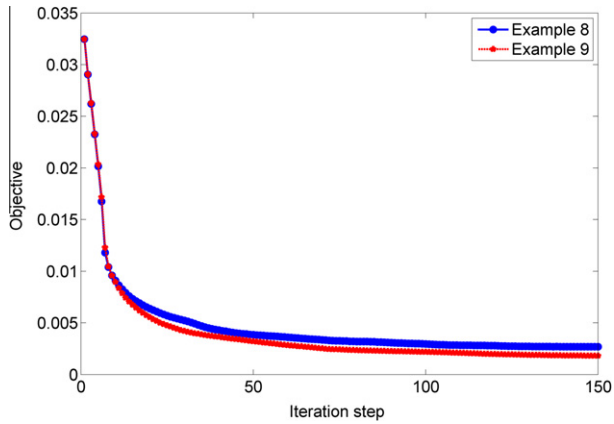


Fig. 7. The convergence histories of the objective functions for Examples 8 and 9.

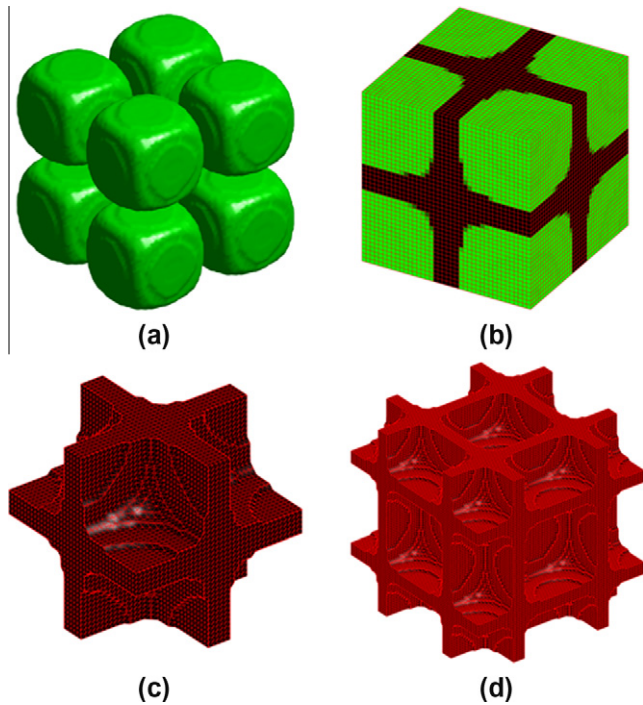


Fig. 8. The microstructure of a cellular composite targeting for the lower HS bound (a) ISO surface ( $\rho^e = 0.90$ ) of the high-transport phase for  $2 \times 2 \times 2$  ranked base cells starting from Initial Design I (Example 10); (b) External surface of an RVE within the center of  $2 \times 2 \times 2$  ranked base cells; (c) The ISO surface of the low-transport phase for the RVE in (b); (d) The ISO surface of the low-transport phase for  $2 \times 2 \times 2$  ranked RVE shown in (b).

ranked base cells and its external surface is shown in Fig. 8b, which illustrates the high-transport phase accumulates at the corners of base cells. The tri-connected low-transport phase (red<sup>1</sup> in Fig. 8c and d) is shaped into a 3D lattice encapsulating the high-transport phase tightly so that the transport function is depressed. The objective function and volume fraction have similar convergent trend to their counterparts in 2D. The attained transport property for this 3D example is  $\text{diag}(\bar{\kappa}) = [1.7772, 1.7767, 1.7768]$ , again reasonably close to its target  $\hat{\kappa} = 1.7500\mathbf{I}$ .

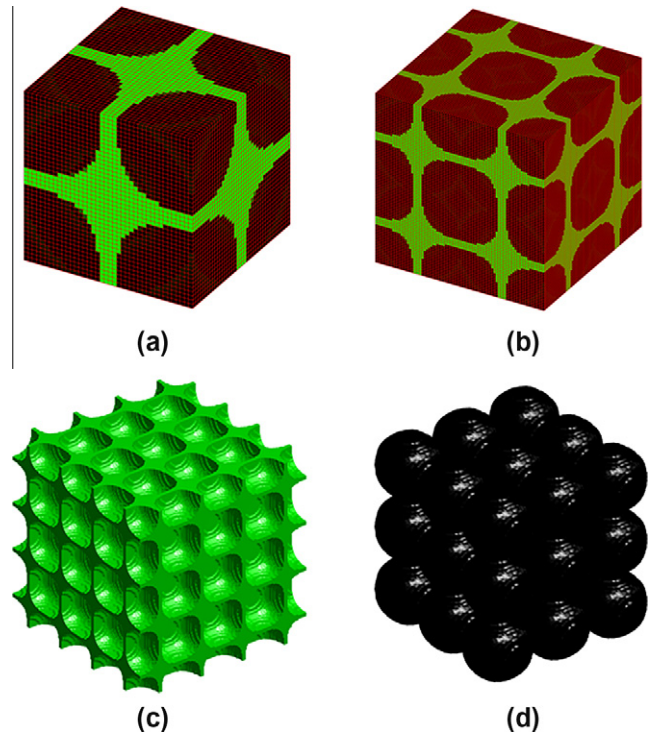


Fig. 9. The microstructure of a composite targeting for upper HS bound (a) External surface of the optimal base cell starting from initial values I (Example 11); (b) The external surface of the  $2 \times 2 \times 2$  ranked base cells; (c) ISO surface ( $\rho^e = 0.90$ ) of the high-transport phase for  $4 \times 4 \times 4$  ranked base cells; (d) Partial ISO surface of the low-transport phase for  $5 \times 5 \times 5$  ranked base cells.

### 3.4. 3D examples targeted for the upper HS bound

The upper HS bound  $\hat{\kappa} = 1.8750\mathbf{I}$  is set as the target in Example 11. Starting from 3D version of Initial Design I, the transport property attains  $\bar{\kappa} = 1.8600\mathbf{I}$  after 150 iterations as shown in Fig. 9a. The high-transport phase (light green) evolves to a tri-connected scaffold so that the transportation can be made most efficiently. The low-transport phase is encapsulated in the cellular composite attaining the upper HS bound, resulting in evenly distributed cubic inclusions with round corners (Fig. 9d). This phenomenon of swapping the phases between the upper and lower HS bounds has already been observed in the 2D cases (Figs. 2c and Fig. 5c). To illustrate the inner microstructure of the composite in detail, the ISO-surfaces for high- and low-transport phases are plotted in Figs. 9c–d, respectively, in a periodically ranked PBC cellular assembly.

### 3.5. Fabrication with Solid Free-From Fabrication techniques

3D multi-material printing signifies a cutting-edge additive manufacturing technology and has drawn some attention recently [48]. In this paper, several cellular material designs were selected and created by stereolithographic apparatus (SLA). Similar to other solid free-from fabrication techniques, it builds up 3D objects in a layer-by-layer process by scanning a UV laser over a photopolymerizable liquid. Importantly, recent developments have allowed printing multiple materials in the same layer. Therefore this technology is used in this study to fabricate the biphasic microstructural samples.

Specifically, the Connex500™ Multi-Material 3D Printing System (innovated by Objet Geometries Inc.), the 3D commercially available SFF technologies allowing multi-material fabrication,

<sup>1</sup> For interpretation of color in Figs. 8 and 9, the reader is referred to the web version of this article.

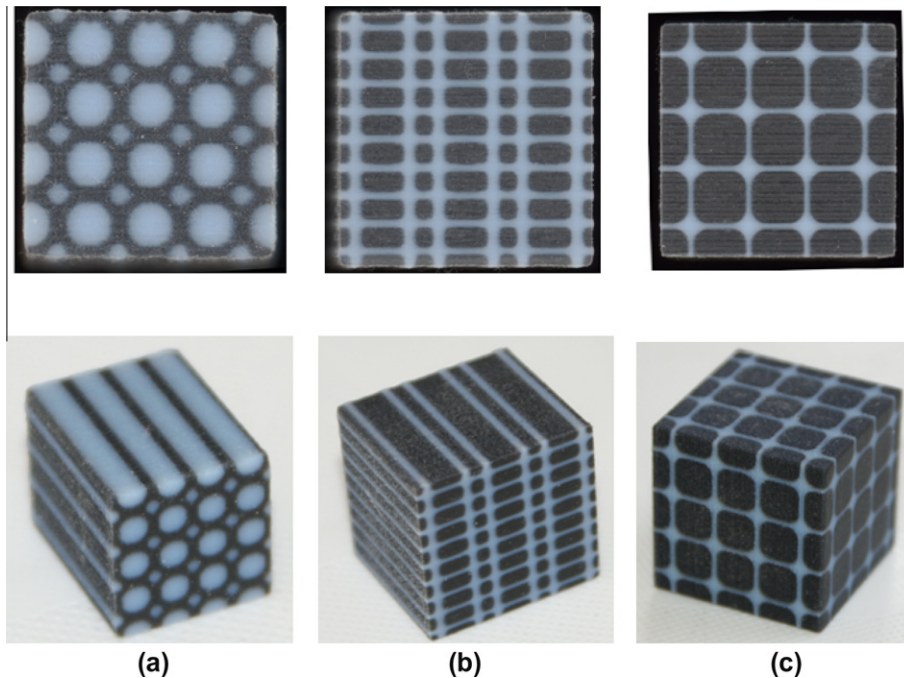


**Fig. 10.** Fabricated material samples for (a) Example 2; (b) Example 6; (c) Example 9. (the top and bottom subfigures are the cross-sections and 3D-views of the fabricated material samples).

was employed in our work. However, this technology has not featured in the literature to date, and its use in fabricating the designed biphasic structures is considered promising for cellular materials.

The Connex500™ Multi-Material 3D Printing System is used to fabricate multi-material samples based on selected material designs from the above sections. Solid CAD models are required to interface with the Connex500™. The 3D CAD Design software, SolidWorks, is used to translate the optimized topology models in an appropriate format. For 2D designs, a bitmap of the microstructure can be imported as a background and the splines can be used to obtain geometrical features which accurately reflect the original microstructural topology. To create 3D objects, the 2D representation can be extruded to create a representative 3D material model. For 3D designs, the dimensions of the geometrical features were captured from the original MATLAB finite element representation, allowing 1 element to represent 1 unit length. For instance, the matrix wall has a width of 4 units and the chamfer on the square inclusion is approximately equal to 10 units. Once the models were constructed, a scale factor was applied so that the smallest feature (600 $\mu\text{m}$ ) can be attained for Connex500™. To match the high and low thermal conductivities in the following samples, TangoBlack and VeroWhite were used as raw materials in Connex500™ system. Both of them are acrylic-based photopolymer materials but have rubber-like flexible (TangoBlack) and rigid (VeroWhite) properties, respectively.

The images of some real samples are presented in Fig. 10, with the top and bottom parts depicting the cross-section and 3D-view of these materialized examples. The subfigures of Fig. 10a–c are corresponded to Examples 2, 6 and 9, respectively. It is apparent from these images that the features of the microstructural designs are accurately captured in the SLA fabrication process. The interfaces are clear in each case, as is evident in the cross-sectional images. The ability to accurately fabricate these sophisticated cellular materials using commercially available SLA technology provides an important link between theoretical and experimental approaches. However, validating

theoretical design and predictions via experiment is left to subsequent research.

#### 4. Conclusions

This paper deals with the design of 2D and 3D periodic microstructural composites using a modified Bidirectional Evolutionary Structural Optimization (BESO) method. Following a sensitivity analysis, the elements are ranked relative to lower and upper sensitivity sets for materials addition or removal. Unlike the traditional element-based BESO methods, this modified BESO characterizes a step-wise change in elemental volume fraction with a reduced step size, which allows altering a larger portion (up to 50%) of elements in a single step. This modification makes the algorithm more like an Optimality Criteria (OC) method and the benchmark examples showed that it converges to the optimum properly. With this improved BESO method, we obtained classical Vigdergauz-like structures and Kagomé lattices, both of them are well-known for their superior transport properties in various physical scenarios. All these examples, with different initial values, design domains, target values, demonstrated that this modified BESO method is competent in material design and has potential to be applied to other areas in topology optimization.

As part of this paper, we also showed that these complex biphasic microstructural materials can be fabricated by a Connex500™ Multi-Material 3D Printing System. Being a commercially available Stereo Lithographic Apparatus, it accurately replicated the geometries of several complex material designs. The ability to fabricate such complicated microstructural materials forms an important bridge between theoretical design and sample prototyping.

#### Acknowledgments

The financial supports from Australian Research Council are gratefully acknowledged. The first author wishes to acknowledge the support from the opening fund (30915002) in the State Key

Laboratory of Advanced Technology for Vehicle Design & Manufacture, Hunan University, China.

**Appendix A. MATLAB code**

A short MATLAB code is provided herein to facilitate the comprehension and implementation of this present algorithm. Before running this program, one needs to define the mesh size factors  $n_x$  and  $n_y$ , the weighting factor  $\zeta$  for nonlinear diffusion energy, the vol-

ume constraint  $vol$  for the base cell, the initial step size  $move$  for the design variables in each iteration, weighting factors  $r_1$  and  $r_2$ , the isotropic properties  $k_1$  and  $k_2$  for the low-transport and high-transport phases and the threshold coefficient  $\delta$ . The target property is the lower Hashin–Shtrikman bound in 2D (Line 25, based on the lower HS bound Eq. (16)) and the initial values are defined in Line 5. When prescribing the periodic, boundary to make the micro-scale characteristic fields  $\chi(\mathbf{y})$  (obtained by calling FEA function  $FE$  in Line 9) periodic, the nodes on the opposite edges are set to have identical

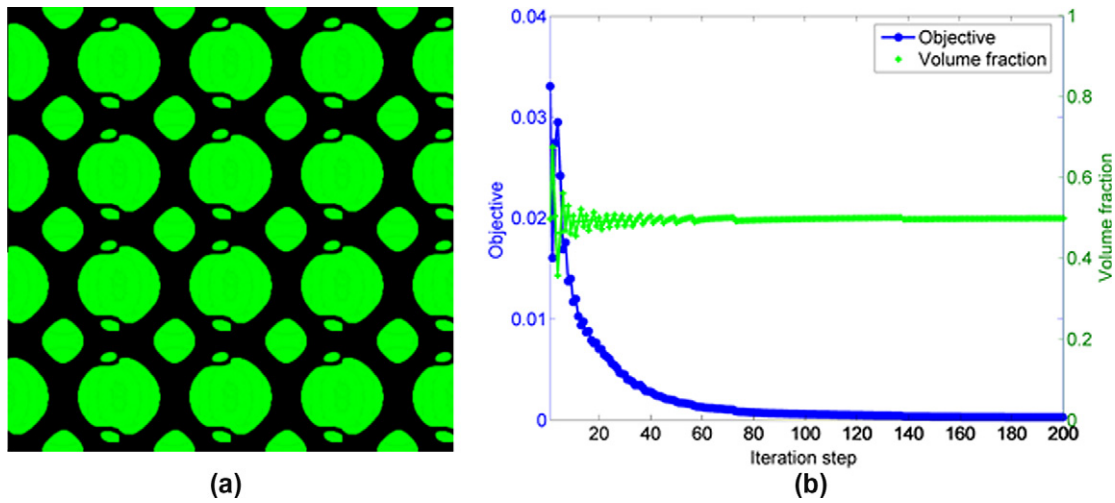


**Fig. A1.** The microstructure of a composite targeting for lower HS bound (a) Base cell in (a) ranking in a  $4 \times 4$  matrix; (d) Base cell in (b) Convergence of the objective function and volume fraction in Example 10.

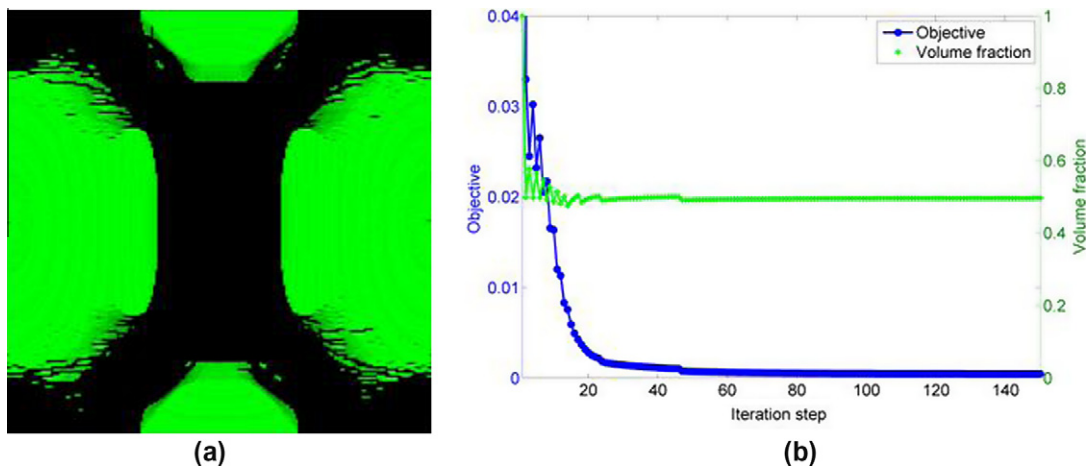


**Fig. A2.** The microstructure of a composite targeting for lower HS bound without nonlinear diffusion: (a) Base cell (b) The convergence of the objective function and volume fraction.

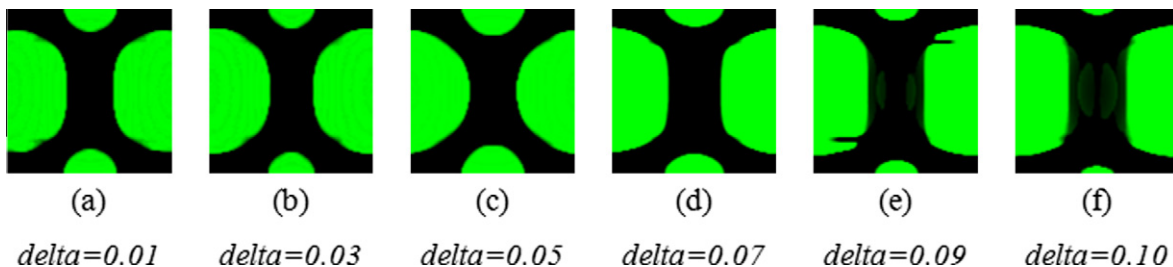


**Fig. A3.** The microstructures with different  $\delta$  but the same  $move$  (0.15) and  $\zeta$  (0.15).

numbers by calling the function *setPBC* (Lines 94–99). The derivatives of characteristic field are obtained in Line 14 by multiplying  $\chi(\mathbf{y})$  with a derivative operator *B*. The effective (homogenized) property Eq. (12) and its sensitivity Eq. (18) are calculated in Lines 17–20. Before applying the BESO method (Lines 29–48), the sensitivity is rectified by the nonlinear diffusion techniques in function *nonDifu* in Lines 49–67. To run this code, one just needs to input BESO(200,200,0.5,0.12,0.1,1,1,3,0.05) in MATLAB command window.

The three main evolving parameters, namely *zeta*, *move* and *delta*, play very important roles for controlling the optimization process. For example, if we call this code as BESO(100,100,0.5,0.2,0.28,1,1,1,3,0.05) in Example 10, a different microstructure from the plot in Fig. 2b is generated as shown in Fig. A1a. The only difference between these two examples is that the value of *move* in Example 10 is 2.8 times larger than the latter. Generally speaking, the larger the *move* is, the more flexible the algorithm would be. But the flexibility may be obtained at the cost of higher risk of

### Initial Designs I:

```
[x0,y0] = meshgrid(-0.5+h/2:h:0.5-h/2,-0.5+h/2:h:0.5-h/2);
rho=sqrt(x0.^2+y0.^2);
```

### Initial Designs II:

```
[x0,y0] = meshgrid(-0.5+h/2:h:0.5-h/2,-0.5+h/2:h:0.5-h/2);
rho=1-sqrt(x0.^2+y0.^2);
```

For three-time horizontally-repeated Initial Designs, the space step *h* in Line 2 should be changed to “*h=1/ny*” and one line should be added after Line 5 as:

```
rho=[rho rho rho];
```

For the examples to attain to upper HS bound, Lines 15, 16 and 25 should be changed to:

### Line 15:

```
dke=-2*k1*(-k1+k2)/(2*k1+rho(ely,elx)*(-k1+k2))-2*(1-rho(ely,elx))*k1*(-k1+k2)^2/(2*k1+rho(ely,elx)*(-k1+k2))^2;
```

### Line 16:

```
kap=(k1+(2*(1-rho(ely,elx))*k1*(k2-k1))/(2*k1+rho(ely,elx)*(k2-k1)))*eye(2);
```

### Line 25:

```
e_obj = k2 + (2*mass(end)*k2*(k1-k2))/(2*k2+(1-mass(end))*(k1-k2)); %HS upper bound
```

```
1. function BESO(nx,ny,vol,zeta,move,r1,r2,k1,k2,delta)
2. h = 1/nx; NE = ny*nx;
3. KE = 1/6*[ 4 -1 -2 -1;-1 4 -1 -2;-2 -1 4 -1;-1 -2 -1 4]; %Elem. matrix
4. B = 0.5*[ 1, -1, -1, 1; 1, 1, -1, -1]; % Derivative matrix B
5. [x0,y0,z0] = sphere(max(nx,ny)-1); rho=vol+0.5*x0(1:ny,1:nx); %Initials

6. mass(1) = 1; obj(1) = 1; %%%%%%%%% START BESO ITERATION %%%%%%%%%
7. while obj(end) >= 1e-4 | abs(mass-vol) >= 1e-4
8.     move = move*0.98; zeta = 0.98*zeta;
9.     [T] = FE(nx,ny,rho,k1, k2,KE); % FE-ANALYSIS

10.    for ely = 1:ny
11.        for elx = 1:nx
12.            edof = getEdof(nx,ny,elx,ely);
13.            T1 = T(edof,1); T2 = T(edof,2);
14.            S1 = B*T1; S2 = B*T2;
15.            dke = 2*k2*(k1-k2)/(2*k2+(1-rho(ely,elx))*(k1-k2)) +
2*rho(ely,elx)*k2*(k1-k2)^2/(2*k2+(1-rho(ely,elx))*(k1-k2))^2;
16.            kap = (k2 + (2*rho(ely,elx)*k2*(k1-k2))/(
(2*k2+(1-rho(ely,elx))*(k1-k2)))*eye(2);
17.            Q1(ely,elx) = kap(1,1)*(1 - S1(1));
18.            Q2(ely,elx) = kap(2,2)*(1 - S2(2));
19.            DQ1(ely,elx) = (1 - S1(1))*dke*(1-S1(1));
20.            DQ2(ely,elx) = (1 - S2(2))*dke*(1-S2(2));
21.        end
22.    end
```

```

23. C = [sum(sum(Q1)), sum(sum(Q2))]/NE;
24. mass = [mass sum(rho(:))/NE];
25. e_obj = (k1 + (2*(1-mass(end))*k1*(k2-k1))/(2*k1 +
mass(end)*(k2-k1))); % Hashin-Shtrikman lower bound
26. A1 = e_obj - C(1); A2 = e_obj - C(2);
27. obj = [obj r1*A1^2 + r2*A2^2];
28. dc = -2*(r1*A1*DQ1 + r2*A2*DQ2) + zeta*nonDifu (rho,nx,ny);

29. %%%%%%%%%% BESO METHOD %%%%%%%%%%%
30. alp_v = sort(dc(:));
31. for q=1:length(alp_v)
32.     [m,n]= find(dc==alp_v(q));
33.     if alp_v(q) > (1+delta)*mean(alp_v)
34.         if mass(end) > vol
35.             if rho(m,n)> move+0.001 rho(m,n)= rho(m,n) - move; end
36.         end
37.     end
38.     if alp_v(q) < (1-delta)*mean(alp_v)
39.         if mass(end) < vol
40.             if rho(m,n) < 1-move rho(m,n)= rho(m,n) + move; end
41.         end
42.     end
43. end

44. if length(obj) >150 obj=obj(2:end); mass=mass(2:end); break; end
45. colormap(gray); imagesc(-rho);
46. axis equal; axis tight; axis off; caxis([-1 0]); pause(1e-6);
47. disp([' Iter: ' sprintf('%3i',length(obj)-1) ' Vol: '
sprintf('%5.4f',mass(end)) ' Obj: ' sprintf('%6.4f',obj(end)) ' Lambda: '
sprintf('%6.4f ',C)]);
48. end

49. %%%Nonlinear Diffusion With German & McClure Function%%%%%%%%%%
50. function [dc2] = nonDifu(f,nx,ny)
51. for j = 1:ny
52.     for i = 1:nx
53.         loop = 0.; Round_Sum = 0; Center = 0.;
54.         for k=max(j-1,1):min(j+1,ny)
55.             for l=max(i-1,1):min(i+1,nx)
56.                 if (k==j & l~=i) | (k ~=j & l==i)
57.                     loop = loop +1;
58.                     t = f(k,l) - f(j,i);
59.                     Direct = 1/(1+t^2)^2;
60.                     Round_Sum = Round_Sum + f(k,l)*Direct;
61.                     Center = Center + Direct;
62.                 end
63.             end
64.         end
65.         dc2(j,i) = -2*(Round_Sum - Center*f(j,i));
66.     end
67. end

68. %%% Finite Element Analysis %%%%%%%%%%%
69. function [T]=FE(nx,ny,rho,k1,k2,KE)

```

```

70. NN = (ny+1)*(nx+1); F = sparse(NN,2);
71. K = sparse(NN,NN); T = zeros(NN,2);
72. for ely = 1:ny
73.     for elx = 1:nx
74.         edof = getEdof(nx,ny,elx,ely);
75.         ke = k2 + (2*rho(ely,elx)*k2*(k1-k2))/(2*k2+(1-rho(ely,elx))*(k1-k2));
76.         Fe = 0.5*[ 1, 1; -1, 1; -1, -1; 1, -1]*ke*eye(2);
77.         K(edof,edof) = K(edof,edof) + ke*KE;
78.         F(edof,:) = F(edof,:) + Fe;
79.     end
80. end

81. fixeddofs = [1:ny ny+1:ny+1:NN NN-ny];
82. alldofs = [1:(nx+1)*(ny+1)];
83. freedofs = setdiff(alldofs,fixeddofs);
84. T(freedofs,:) = K(freedofs,freedofs)\F(freedofs,:);
85. T(1:ny+1,:) = T(nx*(ny+1)+1:NN,:);
86. T(ny+1:ny+1:NN,:) = T(1:ny+1:NN,:);

87. %%%%%%%%% Get Element Nodes %%%%%%%%%
88. function [edof] = getEdof(nx,ny,elx,ely)
89. n1 = setPBC((ny+1)*elx + ely, nx, ny);
90. n2 = setPBC((ny+1)*(elx-1) + ely, nx, ny);
91. n3 = setPBC((ny+1)*(elx-1) + ely + 1, nx, ny);
92. n4 = setPBC((ny+1)*elx + ely + 1, nx, ny);
93. edof = [n1; n2; n3; n4];

94. %%%%%%%%% Prescribing Periodic Boundary %%%%%%%%%
95. function [n] = setPBC(d, nx, ny)
96. n = d;
97. if (d<(ny+1)) n = nx*(ny+1) + d; end
98. if (ceil(d/(ny+1)) == d/(ny+1)) n = d - ny; end
99. if (d==(ny+1) | d==1 | d==(nx+1)*(ny+1)) n = nx*(ny+1) + 1; end

```

instability and slow convergence. Thus, based on the numerical experiments, a proper range of *move* should be in between 0.1 and 0.2. Fig. A1b illustrates the variations of the objective value and the volume fraction for Example 10. It shows that the oscillation of the volume fraction dwindles to zero around 100 iterations. And so is for the objective value.

The value of the nonlinear diffusion weighting factor *zeta* depends on the mesh size. Larger value will make the diffusion role more dominant, leading to blur edges. But if its value drops gradually, as shown in line 8, the nonlinear diffusion role becomes weaker and weaker and the intermediate density can be suppressed finally. Another advantage of an asymptotic change of nonlinear diffusion factor is that mesh-dependency can be avoided. The role of nonlinear diffusion can be validated by setting the weighting factor *zeta* = 0 when running the attached code with the command BESO(200,200,0.5,0,0.1,1,1,1,3,0.05), which makes the sensitivity follow Eq. (18). Compared with the Example 2 using the sensitivity of Eq. (21), the result shown in Fig. A2a has immethodical boundaries, hardly to be fabricated. The obtained effective transport property is  $\text{diag}(\bar{\kappa}) = [1.6904, 1.6875]$ , which is a bit away from the target 1.6667 compared with  $\text{diag}(\bar{\kappa}) = [1.6759, 1.6737]$  in Example 2. Furthermore, the sensitivity defined in Eq. (21) seems more sensitive than the one in Eq. (18) as it makes the optimization converge quickly if comparing the convergence histories shown in Fig. 3 and A2b.

Parameter *delta* defines how many elements are allowed to change their densities in each iteration step. In Fig. A3, a series of microstructures with different *delta* (0.01–0.1) but the same *move* (0.15) and *zeta* (0.15) are illustrated. If it equals zero, all elements

join the updating process. But larger *delta* could make some *dead* region in the design domain, where the local densities never change and keep the initial intermediate state (e.g. the microstructures in Fig. A3e–f for *delta* = 0.09 and 0.10). Like the *move* parameter, larger *delta* also increases the flexibility of the algorithm and makes it possible to seek for the multiple solutions (e.g. *delta* = 0.09 in Fig. A3e). Based on the examples in Fig. A3, the suggested *delta* should be less than 0.05 but a larger value might be feasible in some cases.

This attached code can also handle rectangle design domain by setting *nx* and *ny* differently. Although the microstructures look asymmetry, their effective transport properties are indeed isotropic. For these kinds of microstructures, readers only need to call this code as BESO(100,50,0.5,0.2,0.1,1,1,1,3,0.0) or other different values of *nx* and *ny*.

Except for Example 2, other 2D examples can be obtained by simply changing Line 5 for initial values, line 15–16 for interpolation scheme and its derivative, and Line 25 for the objective value. The other two initials can be defined in Line 5:

## References

- [1] M.P. Bendsøe, O. Sigmund, Topology, optimisation: theory, methods, and applications, Springer, Berlin, 2003.
- [2] O. Sigmund, Materials with prescribed constitutive parameters - an inverse homogenization problem, Int. J. Solids Struct. 31 (1994).
- [3] A. Bensoussan, G. Papanicolaou, J.L. Lions, Asymptotic Analysis for Periodic Structures, North Holland, Amsterdam, 1978.
- [4] M.P. Bendsøe, N. Kikuchi, Generating optimal topologies in structural design using a homogenization method, Comput. Methods Appl. Mech. Eng. 71 (2) (1988) 197–224.

- [5] J.E. Cadman, S.W. Zhou, Y.H. Chen, Q. Li, On design of multifunctional microstructural materials, *J. Mater. Sci.* in press, Doi: 10.1007/s10853-012-6643-4.
- [6] S. Osher, J.A. Sethian, Front propagating with curvature dependent speed: algorithms based on Hamilton–Jacobi formulations, *J. Comput. Phys.* 78 (1988) 12–49.
- [7] M.Y. Wang, X.M. Wang, D.M. Guo, A level set method for structural topology optimization, *Comput. Methods Appl. Mech. Eng.* 192 (1–2) (2003) 227–246.
- [8] S.W. Zhou, Q. Li, A variational level set method for the topology optimization of steady-state Navier–Stokes flow, *J. Comput. Phys.* 227 (2008) 10178–10195.
- [9] W. Prager, J.E. Taylor, Problems of optimal structural design, *J. Appl. Mech.* 35 (1968) 102–106.
- [10] J.H. Holland, *Adaptation in Natural and Artificial Systems*, University of Michigan Press, Ann Arbor, 1975.
- [11] Y.M. Xie, G.P. Steven, A simple evolutionary procedure for structural optimization, *Comput. Struct.* 49 (5) (1993) 885–896.
- [12] Y.M. Xie, G.P. Steven, *Evolutionary Structural Optimization*, Springer, London, 1997.
- [13] Q. Li, G.P. Steven, Y.M. Xie, Displacement minimization of thermoelastic structures by evolutionary thickness design, *Comput. Methods Appl. Mech. Eng.* 179 (3–4) (1999) 361–378.
- [14] X.Y. Yang, Y.M. Xie, G.P. Steven, O.M. Querin, Bidirectional evolutionary method for stiffness optimization, *AIAA J.* 37 (11) (1999) 1483–1488.
- [15] X. Huang, Y.M. Xie, M.C. Burry, A new algorithm for bi-directional evolutionary structural optimization, *JSME Int. J. Series C-Mech. Sys. Mach. Elem. Manufact.* 49 (4) (2006) 1091–1099.
- [16] X. Huang, Y.M. Xie, M.C. Burry, Advantages of bi-directional evolutionary structural optimization (ESO) over evolutionary structural optimization (ESO), *Adv. Struct. Eng.* 10 (6) (2007) 727–737.
- [17] X. Huang, Y.M. Xie, A new look at ESO and BESO optimization methods, *Struct. Multidiscip. Optim.* 35 (1) (2008) 89–92.
- [18] Q. Li, G.P. Steven, Y.M. Xie, A simple checkerboard suppression algorithm for evolutionary structural optimization, *Struct. Multidiscip. Optim.* 22 (3) (2001) 230–239.
- [19] G.P. Steven, Q. Li, Y.M. Xie, Evolutionary topology and shape design for general physical field problems, *Comput. Mech.* 26 (2) (2000) 129–139.
- [20] O.M. Querin, G.P. Steven, Y.M. Xie, Evolutionary structural optimization (ESO) using a bi-directional algorithm, *Eng. Comput.* 15 (1998) 1031–1048.
- [21] X. Huang, Y.M. Xie, *Evolutionary Topology Optimization of Continuum Structures: Methods and Applications*, John Wiley and Sons, Chichester, 2010.
- [22] T. Gao, W.H. Zhang, J.H. Zhu, Y.J. Xu, D.H. Bassir, Topology optimization of heat conduction problem involving design-dependent heat load effect, *Finite Elem. Anal. Des.* 44 (2008) 805–813.
- [23] O.Q. Liang, Performance-based optimization: a review, *Adv. Struct. Eng.* 10 (6) (2007) 739–753.
- [24] Q.Q. Liang, G.P. Steven, Y.M. Xie, Optimal topology selection of continuum structures with displacement constraints, *Comput. Struct.* 77 (6) (2000) 635–644.
- [25] Q. Li, G.P. Steven, O.M. Querin, Y.M. Xie, Shape and topology design for heat conduction by evolutionary structural optimisation, *Int. J. Heat Mass Transfer* 42 (17) (1999) 3361–3371.
- [26] Q. Li, G.P. Steven, Y.M. Xie, O.M. Querin, Evolutionary topology optimization for temperature reduction of heat conducting fields, *Int. J. Heat Mass Transfer* 47 (23) (2004) 5071–5083.
- [27] O.M. Querin, V. Young, G.P. Steven, Y.M. Xie, Computational efficiency and validation of bi-directional evolutionary structural optimisation, *Comput. Methods Appl. Mech. Eng.* 189 (2) (2000) 559–573.
- [28] V. Young, O.M. Querin, G.P. Steven, Y.M. Xie, 3D and multiple load case bi-directional evolutionary structural optimization (BESO), *Struct. Optim.* 18 (1999) 183–192.
- [29] S.W. Zhou, Q. Li, The relation of constant mean curvature surfaces to multiphase composites with extremal thermal conductivity, *J. Phys. D Appl. Phys.* 40 (19) (2007) 6083–6093.
- [30] S.W. Zhou, Q. Li, A microstructure diagram for known bounds in conductivity, *J. Mater. Res.* 23 (3) (2008) 798–811.
- [31] S.W. Zhou, Q. Li, Computational design of multiphase microstructural materials for extremal conductivity, *Comput. Mater. Sci.* 43 (2008) 549–564.
- [32] Z. Hashin, S. Shtrikman, A variational approach to theory of effective magnetic permeability of multiphase materials, *J. Appl. Phys.* 33 (10) (1962) 3125–3131.
- [33] E.J. Haug, K.K. Choi, V. Komkov, *Design Sensitivity Analysis of Structural Systems*, Academic Press, Orlando, 1986.
- [34] O. Sigmund, A 99 line topology optimization code written in Matlab, *Struct. Multidiscip. Optim.* 21 (2) (2001) 120–127.
- [35] M.Y. Wang, S. Zhou, H. Ding, Nonlinear diffusions in topology optimisation, *Struct. Multidiscip. Optim.* 28 (4) (2004) 262–276.
- [36] Y.H. Chen, S.W. Zhou, Q. Li, Computational design for multifunctional microstructural composites, *Int. J. Mod. Phys. B* 23 (2008) 1345–1351.
- [37] Y.S. Song, J.R. Youn, Evaluation of effective thermal conductivity for carbon nanotube/polymer composites using control volume finite element method, *Carbon* 44 (4) (2006) 710–717.
- [38] M. Wang, N. Pan, Modeling and prediction of the effective thermal conductivity of random open-cell porous foams, *Int. J. Heat Mass Transfer* 51 (2008) 1325–1331.
- [39] O. Wiener, *Abh. Math.-Phys. Klass Königl. Sächsh. gesel. wissen*, 32 (1912) 509.
- [40] Y. Liu, F. Jin, Q. Li, S.W. Zhou, A fixed-grid bidirectional evolutionary structural optimization method and its applications in tunnelling engineering, *Int. J. Numer. Methods Eng.* 73 (12) (2008) 1788–1810.
- [41] S. Vigdergauz, 2-dimensional grained composites of extreme rigidity, *J. Appl. Mech., Trans. ASME* 61 (2) (1994) 390–394.
- [42] J.K. Guest, J.H. Prévost, Design of maximum permeability material structures, *Comput. Methods Appl. Mech. Eng.* 196 (4–6) (2007) 1006–1017.
- [43] I. Syozi, Statistics of Kagome lattice, *Progress Theoret. Phys.* 6 (3) (1951) 306–308.
- [44] P.W. Anderson, Ordering and antiferromagnetism in ferrites, *Phys. Rev.* 102 (4) (1956) 1008–1013.
- [45] M.J. Higgins, Y. Xiao, S. Bhattacharya, P.M. Chaikin, S. Sethuraman, R. Bojko, D. Spencer, Superconducting phase transitions in a kagome wire network, *Phys. Rev. B* 61 (2) (2000) R894–R897.
- [46] S. Hyun, S. Torquato, Optimal and manufacturable two-dimensional, Kagome-like cellular solids, *J. Mater. Res.* 17 (1) (2002) 137–144.
- [47] J.K. Carson, S.J. Lovatt, D.J. Tanner, A.C. Cleland, Thermal conductivity bounds for isotropic, porous materials, *Int. J. Heat Mass Transfer* 48 (2005) 2150–2158.
- [48] J. Hiller, H. Lipson, Design and analysis of digital materials for physical 3D voxel printing, *Rapid Prototyp. J.* 15 (2009) 137–149.